A vitamin D-based strategy overcomes chemoresistance in prostate cancer

Kateryna Len-tayon, Claire Beraud, Clara Fauveau, Anna Y Belorusova, Yassmine Chebaro, Antonio Mouriño, Thierry Massfelder, Anne Chauchereau, Daniel Metzger, Natacha Rochel, et al.

Received: 29 November 2023 | Revised: 16 May 2024 | Accepted: 29 May 2024

DOI: 10.1111/bph.16492

RESEARCH ARTICLE

A vitamin D-based strategy overcomes chemoresistance in prostate cancer

Kateryna Len-Tayon[1,2,3,4] | Claire Beraud[5] | Clara Fauveau[1,2,3,4,6] | Anna Y. Belorusova[1,2,3,4] | Yassmine Chebaro[1,2,3,4] | Antonio Mouriño[7] | Thierry Massfelder[8] | Anne Chauchereau[9] | Daniel Metzger[1,2,3,4] | Natacha Rochel[1,2,3,4] | Gilles Laverny[1,2,3,4]

[1]Institute of Genetics and Molecular and Cellular Biology (IGBMC), Illkirch-Graffenstaden, France

[2]CNRS UMR 7104, Illkirch-Graffenstaden, France

[3]Inserm U1258, Illkirch-Graffenstaden, France

[4]University of Strasbourg, Illkirch-Graffenstaden, France

[5]Urosphere, Toulouse, France

[6]Transgene SA, Illkirch-Graffenstaden, France

[7]Department of Chemistry, University of Santiago de Compostela, Santiago de Compostela, Spain

[8]INSERM U1260, Strasbourg, France

[9]INSERM U981, Gustave Roussy, University of Paris-Saclay, Villejuif, France

Correspondence
Gilles Laverny, Institute of Genetics and Molecular and Cellular Biology (IGBMC), 1 rue Laurent Fries, Illkirch-Graffenstaden 67400, France.
Email: laverny@igbmc.fr

Present address
Anna Y. Belorusova, Department of assay development and screening, Zobio B.V., Leiden, The Netherlands.

Funding information
This work was funded by Inserm and the Canceropole Est to G.L., by the Ligue Contre le Cancer Est to D.M., by the SATT Conectus to G.L. and D.M., by the Association pour La Recherche sur les Tumeurs Prostatiques (ARTP) to N.R. and by Institut National du Cancer to D.M. and T.M.. K.L. is supported by the Ministry of Higher Education and Research and the Fondation ARC pour la Recherche sur le Cancer. C.F. is supported by the Ministry of Higher Education and Research. The research

Background and purpose: Castration-resistant prostate cancer (CRPC) is a common male malignancy that requires new therapeutic strategies due to acquired resistance to its first-line treatment, docetaxel. The benefits of vitamin D on prostate cancer (PCa) progression have been previously reported. This study aimed to investigate the effects of vitamin D on chemoresistance in CRPC.

Experimental approach: Structure function relationships of potent vitamin D analogues were determined. The combination of the most potent analogue and docetaxel was explored in chemoresistant primary PCa spheroids and in a xenograft mouse model derived from a patient with a chemoresistant CRPC.

Key results: Here, we show that Xe4MeCF3 is more potent than the natural ligand to induce vitamin D receptor (VDR) transcriptional activities and that it has a larger therapeutic window. Moreover, we demonstrate that VDR agonists restore docetaxel sensitivity in PCa spheroids. Importantly, Xe4MeCF3 reduces tumour growth in a chemoresistant CRPC patient-derived xenograft. In addition, this treatment targets signalling pathways associated with cancer progression in the remaining cells.

Abbreviations: AR, androgen receptor; CI, combination index; CRPC, castration-resistant prostate cancer; KEGG, Kyoto Encyclopedia of Genes and Genomes; LBD, ligand binding domain; MD, molecular dynamic; MSigDB, molecular signature database; PCa, prostate cancer; PDX, patient-derived xenograft; TUNEL, terminal deoxynucleotidyl transferase dUTP nick end labelling; VDR, vitamin D receptor.

Claire Beraud and Clara Fauveau contributed equally.

also was funded by the French National Research Agency (Agence Nationale de la Recherche; ANR) through the Programme d'Investissement d'Avenir under contract ANR-10-LABX-0030-INRT grant under the frame programme Investissement d'Avenir ANR-10-IDEX-0002-02 as well as by the Interdisciplinary Thematic Institute IMCBio, as part of the ITI 2021-2028 program of the University of Strasbourg, CNRS and Inserm; by IdEx Unistra (ANR-10-IDEX-0002); and by SFRI-STRAT'US project (ANR 20-SFRI-0012) and EUR IMCBio (ANR-17-EURE-0023) under the framework of the French Investments for the Future Program.

Conclusion and implications: Taken together, these results unravel the potency of VDR agonists to overcome chemoresistance in CRPC and open new avenues for the clinical management of PCa.

KEYWORDS
castration resistant prostate cancer, docetaxel resistance, patient-derived xenografts, spheroids, vitamin D analogues

1 | INTRODUCTION

Prostate cancer (PCa) is the most frequent visceral neoplasm and the second leading cause of cancer-related death in men in western societies (Siegel et al., 2024). Androgen deprivation therapies are the gold standard for advanced PCa, but they impact the quality of life and lead to castration-resistant prostate cancer (CRPC), the most aggressive subtype of PCa, in many patients. The treatment of choice for CRPC is **docetaxel**, but the median overall survival is only about 2 years (Galsky & Vogelzang, 2010). Resistance to this first-line chemotherapy is a major clinical burden. Thus, there is an urgent need to identify therapeutic strategies to improve the clinical management of docetaxel-resistant CRPC.

The bioactive form of **vitamin D**, 1α,25-dihydroxyvitamin D3 (1,25D3), elicits its effects by binding to the vitamin D nuclear receptor (**VDR**) (Bikle & Christakos, 2020). 1,25D3 and VDR play key roles in calcium homeostasis, as well as in adaptive/innate immune responses, cell growth, differentiation and apoptosis, indicating that 1,25D3 is an option not only for the treatment of bone disorders but also for autoimmune diseases, graft rejection and cancers (Bikle & Christakos, 2020; Feldman et al., 2014). Low 1,25D3 circulating levels and disrupted VDR transcriptional activities have been shown to contribute to PCa progression (Murphy et al., 2014; Siddappa et al., 2023). Numerous pre-clinical in vitro studies reported a synergistic effect of chemotherapy in combination with vitamin D in PCa (Hershberger et al., 2001; Ting et al., 2007). In addition, vitamin D analogues reverse **paclitaxel** resistance in breast cancer, as well as **cisplatin** resistance in squamous cell carcinoma (Attia et al., 2020; Huang et al., 2019). The results obtained in the phase 2 Androgen-Independent Prostate Cancer Study of Calcitriol Enhancing Taxoter (ASCENT) trial using DN-101, a high dose (15 μg) capsule of 1,25D3 that does not induce hypercalcaemia, indicated that 1,25D3 enhances docetaxel activity (Beer, 2005; Trump, 2018). However, the larger ASCENT phase III study used a higher docetaxel regimen in the 1,25D3-treated arm compared with the placebo arm, resulting in an increase docetaxel toxicity (i.e. gastrointestinal, blood and lymph node disorders) and the halt of the study (Scher et al., 2011; Trump, 2018).

What is already known

- The bioactive form of vitamin D has anti-cancer activities but of limited clinical use.
- Vitamin D in combination with chemotherapy has synergistic activities on advanced cancers.

What does this study add

- This study provides a functional and structural characterization of a novel potent vitamin D analogue.
- This vitamin D analogue can overcome docetaxel resistance in AR− and AR+ prostate cancers.

What is the clinical significance

- Vitamin D analogues and docetaxel combination represents a promising strategy to reduce prostate cancer progression.

Thus, the effects of vitamin D on docetaxel resistance in PCa remain to be clarified.

1,25D3 therapeutic doses promote calcium absorption leading to hypercalcaemia (Beer, 2005). More than 4000 vitamin D analogues were synthetized to dissociate the procalcaemic to the anti-inflammatory and/or antiproliferative activities (Laverny et al., 2009; Okamoto et al., 2012). We previously synthetized and characterized Xe4, a 1,25D3 analogue bearing a rigid locked side chain with a diyne moiety [21-nor-calcitriol-20(22),23-diyne], which is more potent than 1,25D3 to induce VDR transcriptional activities (Pérez-García et al., 2003; Rochel et al., 2007). Because the characterization of Xe4 binding properties revealed the presence of a spatial volume around its carbon C17 (Rochel et al., 2007), we designed and synthetized

Xe4Me bearing a methyl moiety at C17 (Sigüeiro et al., 2018). Moreover, because fluorine atoms increase the affinity of the analogues for VDR and their resistance towards metabolic degradation (Eelen et al., 2008; Tanaka et al., 1984), we synthesized Xe4MeCF3 (Sigüeiro et al., 2018), which bears substitutions of the Xe4Me geminal methyl groups by trifluoromethyls in the side chain, and then undertook this study to characterize its activities.

2 | METHODS

2.1 | Materials

1,25-Dihydroxyvitamin D3 (1,25D3 [416.64 g·mol^{-1}], Sigma-Aldrich, 17936), Xe4 (394.5 g·mol^{-1}), Xe4Me (408.5 g·mol^{-1}) and Xe4MeCF3 (516.5 g·mol^{-1}, Sigüeiro et al., 2018) were dissolved in absolute ethanol at 10^{-2} M and stored at −20°C. For oral administration, Xe4MeCF3 was dissolved in sunflower oil and stored at +4°C for up to 2 weeks. For cultured cells, docetaxel (Merck, 01885) was dissolved in DMSO at 10^{-2} M and stored at −20°C. For IP administration, docetaxel (MedChemExpress, HY-B0011A, batch 57-004) was dissolved at 20 mg·ml^{-1} in a solution containing 50% Tween 80 and 50% ethanol and diluted at 4 mg·ml^{-1} in NaCl 0.9%.

2.2 | Biochemistry, crystallization and structure determination

The cDNA encoding His-tagged zVDR LBD (156–453) was cloned into pET28b. The recombinant proteins were produced in *Escherichia coli* BL21 DE3, grown overnight (ON) at 18°C after induction with 1-mM IPTG (OD600 of ∼0.7). Soluble proteins were purified on a Ni Hitrap FFcrude column (Cytiva), followed by His-tag removal by thrombin cleavage and by size exclusion chromatography on a HiLoad Superdex 75 column (Cytiva) equilibrated in Tris 20 mM pH 7, NaCl 200 mM, TCEP 1 mM. The proteins were concentrated to 3–7 mg·ml^{-1} with an Amicon Ultra 30 kDa MWCO. Purity and homogeneity of the proteins were assessed by SDS-PAGE and Native PAGE. The concentrated protein was incubated with a two-fold excess of ligand and a three-fold excess of the coactivator. Crystals were obtained with NCoA2 peptide (KHKILHRLLQDSS) in the presence of Xe4Me and with NCoA1 peptide (RHKILHRLLQEGSPS) in the presence of Xe4MeCF3. The crystallization experiments were carried out by hanging drop vapour diffusion at 290 K by mixing equal volume (1 µl) of protein-ligand complex and reservoir solution (0.1-M BTP pH 7.0, 3-M NaOAc). The crystals of the complex were transferred to artificial mother liquor containing 15% glycerol and flash cooled in liquid nitrogen. Data from crystals of zVDR-Xe4Me and of zVDR-Xe4MeCF3 were collected on the ID30 beamline at ESRF synchrotron and the Proxima2 beamline at Soleil synchrotron, respectively. The raw data of zVDR-Xe4MeCF3 were processed and scaled with the HKL2000 program suite (Otwinowski & Minor, 1997). The raw data of zVDR-Xe4Me were processed with XDS (Kabsch, 2010) and scaled with AIMLESS (Evans, 2006). The structures were solved and refined using Buster (Smart et al., 2012) and Phenix (Adams et al., 2010) and iterative model building using COOT (Emsley & Cowtan, 2004).

2.3 | Molecular dynamics (MD)

For all of structures, 4 glycine (G) residues were added in the missing loop (residues 191–250 of zebrafish VDR) of the crystal structures of the complexes using Modeler. MD calculations were performed using NAMD software (Phillips et al., 2005) and the CHARMM all-atom force field, version 36 (MacKerell et al., 1998). Non-bonded interactions were truncated at a 14-Å cutoff distance, using switch and shift functions for van der Waals and electrostatic forces, respectively. A cubic simulation cell was created around the complex, filled with water, and all charges were negated by addition of Na^+ and Cl^- to yield 0 net charge. MD simulations were initiated with two rounds of energy minimization and heating, and the atomic coordinates of the protein complex were fixed. In the first phase, water was minimized by 1000 steps of conjugate gradient (CG) and heated to 600 K. In the second phase, the water was minimized by 250 steps of CG, followed by heating to 300 K. The constraints on the protein were removed, and the entire system was subjected to energy minimization through 2000 steps of CG and subsequent heating to 300 K. The system was equilibrated for 150 ps. With a 1-fs time step, the production phase extended over a total of 100 ns. The first 10 ns of the simulations required for system equilibration were removed. For each complex, five independent 100-ns MD simulations were computed and averaged, and the MD trajectories at the residue level interactions were analysed, with a distance threshold of 3.5 Å. The protein–ligands contacts were analysed by calculating the averaged contact probabilities at the end of the averaged simulations. Binding free energy decomposition calculations were performed on 100-ns simulations of each complex and repeated five times by MM/GBSA procedure (Kollman et al., 2000) using the CHARMM program.

2.4 | Cell lines

COS7 (ATCC, CRL-1651, RRID:CVCL_0224) and HEK 293 EBNA (Invitrogen, R620-07, RRID:CVCL_6974) cells were grown in Dulbecco's modified Eagle's medium (DMEM) 1 g·L^{-1} glucose supplemented with 10% charcoal-treated FCS and 40 µg·ml^{-1} gentamycin. IEC-18 rat intestinal epithelial cells (ATCC, CRL-1589, RRID:CVCL_0342) were grown in DMEM 4.5 g·L^{-1} glucose supplemented with 5% fetal calf serum (FCS), 1-mM sodium pyruvate, 0.1 UI·ml^{-1} insulin and 40 µg·ml^{-1} gentamycin. MCF-7 breast cancer cells (ATCC, HTB-22, RRID:CVCL_0031) were grown in DMEM 1 g·L^{-1} glucose supplemented with 10% of FCS, 0.6 µg·ml^{-1} insulin and 40 µg·ml^{-1} gentamycin. DU-145 PCa cells (ATCC, HTB-81, RRID:CVCL_0105) were cultured in DMEM 4.5 g·L^{-1} glucose supplemented with Glutamax (Gibco), 10% of FBS and 1% penicillin–streptomycin (Gibco). IGR-CaP1 (RRID:CVCL_A018) and IGR-CaP1-R100 (RRID:CVCL_IR45) cells were

cultured in RPMI 1640 supplemented with Glutamax (Gibco), 10% of FBS, 10-nM HEPES and 40 μg·ml^{-1} gentamycin.

2.5 | Mammalian two-hybrid assay

The GAL4 DNA-binding domain cloning vector pM and the activation-domain cloning vector pVP16 are part of the Mammalian Matchmaker Two-Hybrid Assay kit (BD Biosciences Clontech). COS7 cells were transfected with 50 ng of the full-length human VDR fused to VP16 (pVP-VDR) (Eelen et al., 2005), 150 ng of the pG5-LUC reporter plasmid, 50 ng of an expression vector encoding the Gal4 DBD-MED1 nuclear receptor interacting domain (amino acid 510-787) or the Gal4 DBD-NCoA1 NRID (pSG424-SRC-1; amino acid 570-782), 3 ng of the pRL plasmid and 747 ng of the carrier plasmid per well of the 24-well plate. Tested ligands were added 8 h post transfection, and luciferase activities were determined after 48 h of ligand treatment.

2.6 | Transient transfection and luciferase reporter gene assay

At 80% of HEK 293 EBNA cell confluence, 1 μg of pDNA per well was transfected using jetPEI (Polyplus transfection), following the manufacturer's instructions. Cells were transfected with 150 ng of the expression plasmid pSG5-hVDR encoding the full-length receptor, 150 ng of the CYP24A1 luciferase reporter plasmid (Väisänen et al., 2005), 3 ng of the pRL plasmid (Promega) containing the Renilla luciferase gene (transfection and cell viability control) and 697 ng of the carrier plasmid pBlueScript (Stratagene). Eight hours post transfection, the ligands or vehicle were added. Cells were harvested after 18 h incubation with ligands. The amounts of reporter gene product (firefly luciferase) and constitutively expressed Renilla luciferase produced in the cells were measured using Dual-Luciferase® Reporter Assay System (Promega) on a luminometer plate reader LB96P (Berthold Technologies). To control for unwanted sources of variation luminescence of firefly luciferase, values were normalized to the Renilla luciferase activity and expressed as relative light unit (RLU) intensities.

2.7 | Western blotting

Protein isolation was performed on cells harvested in radioimmunoprecipitation assay lysis buffer (RIPA) (50-mM Tris pH 7.5, 1% Nonident P40, 0.5% sodium deoxycholate, 0.1% SDS, 150-mM NaCl, 5-mM EDTA, 1-mM PMSF and phosphatase and protease inhibitor cocktails [PhosphoStop and Complete-Mini EDTA free; Roche]). Cell lysates were cleared by centrifugation at 10,000 g for 10 min at 4°C. Supernatant protein concentrations were determined using Bradford Reagent (Abcam, ab119216) according to the manufacturer's instructions. Equal protein amounts were separated by electrophoresis under denaturing conditions in 10% SDS-PAGE and transferred to nitrocellulose membranes (Trans-blot turbo transfer system, Bio-Rad), following the manufacturer's protocol. Membranes were blocked by 5% nonfat dry milk in 10-mM Tris pH 7.4, 0.05% Tween-20 (TBST) for 1 h at room temperature and incubated overnight with primary antibodies (Table S6) diluted in 5% bovine serum albumin (BSA) in TBST at 4°C. After 1-h incubation with horseradish peroxidase (HRP)-conjugated antibodies diluted in 5% nonfat dry milk in TBS-T (Table S6), membranes were revealed with an enhanced chemiluminescence detection system (ECLplus, GE Healthcare) and an ImageQuant LAS 4000 biomolecular imager (GE Healthcare). Immunodetected proteins were quantified with FIJI/ImageJ distribution Software.

2.8 | Proliferation assay

MCF7 or DU 145 cells were seeded in 96-well plates for 24 h. BrdU was added to plated cells for 2 h, and proliferation assay was performed according to the manufacturer's instructions (Roche Applied Sciences, 11647229001). Absorbances were measured at 370 nm, and proliferation rate was calculated as percentage of vehicle-treated cells. IGR-CaP1 and IGR-CaP1-R100 cells were resuspended in 65% Cultrex RGF BME Type 2 gel (R&D systems, 3533-005-02) in their respective culture medium and seeded in 96-well ultra-low attachment plate (Falcon, 353072) with sustainable amount of culture medium and grown for 96 h. After treatment, spheroid images were acquired using EVOS M5000 (Invitrogen), and spheroids area was quantified using QuPath 0.3.0. Cell Titer Glo® 3D reagent (Promega, G9681) was used according to the manufacturer's protocol. Briefly, the reagent was equilibrated at room temperature before the addition of 50-μl reagent per well. The plate was vigorously shaken for 5 min using the Synergy HTX multimode reader (Biotek, BTS1A) and incubated at room temperature for additional 25 min. Spheroid lysates were transferred in white 96-well plates and the luminescence determined on a luminometer (Promega, GloMax®-Multi Base Instrument, E7031). To control for unwanted sources of variation, cell proliferation data were represented as a percentage of vehicle-treated cells. The drug combination index (CI) was determined using the Loewe reference model of SynergyFinder 2.0 (Ianevski et al., 2020). Deviations between observed and expected responses with positive and negative values denote a synergy (CI > 10).

2.9 | Reverse transcription-quantitative polymerase chain reaction (RT-qPCR)

Total RNA was isolated from cells with TRI Reagent (Molecular Research Center, Inc.), according to the supplier's protocol. RNAs were quantified by spectrophotometry (Nanodrop, Thermo Fisher). Two μg of total RNA was used to synthetize cDNA using random hexamers and the SuperScript IV reverse transcriptase kit (Thermo Fisher, 18090010), following the manufacturer's instructions. Quantitative PCR reactions were performed using the Light Cycler 480 SYBR

Green I Master X2 Kit (Roche) and LightCycler 480 (Roche®), according to the supplier's protocol, and cDNAs concentrations were quantified by a standard curve method. Oligonucleotides are listed in Table S7.

2.10 | Mice

C57BL/6J mice (Charles River Laboratories, France) were housed in a temperature- and light-controlled animal facility and fed ad libitum (Safe diets, D04, France). Ten-week-old male mice were randomized in various groups and administered *per os* with 100 µl of vehicle, 1,25D3 or Xe4MeCF3. Treatments were not done blindly, because the housing cages had to be labelled with the treatments according to the Animal Healthcare service requirement. No anaesthesia and analgesia was used. At the end of the treatment, blood was collected by inferior palpebral vein puncture, and mice were killed by cervical dislocation. All animal experimental protocols followed ARRIVE guidelines (Percie du Sert et al., 2020) and the editorial on reporting animal studies (Lilley et al., 2020), and were conducted in compliance with French and EU regulations on the use of laboratory animals for research and approved by the IGBMC Ethical Committee and the French Ministry for National Education, Higher Education and Research (#10047-2017052615101492).

2.11 | Patient-derived tumour xenografts studies

PDX-G266 generation, development, administrations and euthanasia were performed by Urosphere (Toulouse, France) as described in Beraud et al. (2023). The animal facility was maintained under standardized conditions: artificial 12 h light–dark cycles between 7:00 AM and 7 PM, ambient temperature of 22 ± 2°C and relative humidity maintained at 55 ± 10%. For the in vivo efficacy studies, PDX tumours were harvested from donor mice after euthanasia and cut in 20-mm^3 fragments. Mice aged between 6 and 9 weeks were anaesthetized by i.p. injection of **ketamine** (100 $mg{\cdot}kg^{-1}$) + **xylazine** (10 $mg{\cdot}kg^{-1}$) and implanted into NMRI-Nude mice (NMRI-Foxn1nu/nu, Janvier-Labs, France). When tumours reached a mean volume of 100 mm^3, mice were randomly assigned to the treatment groups. Health status and body weight for all mice were recorded twice weekly to control any adverse effects. Tumour volume (mm^3) was measured with a calliper twice weekly and calculated as [length (mm) × width (mm)2]*π/6. At the end of the experimental phase, serum samples were collected for calcium measurements, mice were killed by cervical dislocation and tumour samples were collected in PFA for paraffin embedding or frozen in liquid nitrogen for RNA/protein analysis. All experiments followed ARRIVE guidelines (Percie du Sert et al., 2020) and were performed according to the European Community Council Directive 2010/63/UE and the French Ministry for Agriculture, Agrifood and Forestry (Decree 2013-118). Experimental protocols were reviewed by CEE-122 Ethical Committee for Protection of Animals used for Scientific Purposes and approved by French Ministry for National Education, Higher Education and Research under the number *APAFIS#14811-2018042316405732 v6*.

2.12 | Serum calcium levels

Collected blood was incubated overnight at 4°C and centrifuged at 400 g for 10 min at 4°C. Serum calcium levels were determined using colorimetric assays (MAK022, Sigma-Aldrich) according to the manufacturer's protocol.

2.13 | Histological examination

PDXs were fixed in 4% PFA overnight at 4°C. Samples were embedded in paraffin, and 10-µm serial sections were cut with a microtome. Sections were prepared for histological analysis by deparaffinization and stained with haematoxylin and eosin (H&E), using standard protocols.

2.14 | Immunohistochemistry

Five-µm sections of paraffin embedded PDXs were deparaffinized according to standard protocols. Antigen retrieval was performed using SignalStain® Citrate Unmasking Solution (10X) (CST 14746) in a pressure cooker for 20 min. Sections were treated with 3% (v/v) H_2O_2. Non-specific antigens were blocked by 5% nonfat dry milk (m/v) in 10-mM Tris pH 7.4, 0.05% Tween-20 (TBST) for 1 h at room temperature. Immunostaining was performed by overnight incubation at 4°C with primary antibodies in PBS (Table S6). Corresponding Signal Boost IHC Detection HRP-conjugated secondary antibody was added for 30 min at room temperature. Antigen detection was performed using DAB substrate kit (Cell Signaling, #8059), and slides were stained by haematoxylin, as per standard protocols. Sections processed in the absence of primary antibodies were used as negative control.

2.15 | TUNEL assay

Five-µm sections of paraffin embedded PDXs were deparaffinized according to standard protocols and analysed with the In Situ Cell Death Detection Kit, Fluorescein (reference: 11684795910; Roche) following the manufacturer's instructions. Fluoromount-G Mounting Medium with 4′,6-diamidino-2-phenylindole (**DAPI**) (Invitrogen; 00-4959-52) was applied before microscopic acquisition.

2.16 | Image acquisition

The slides were scanned using Brightfield lighting at 20× magnification with a NanoZoomer S210 Digital slide scanner. The NDP.view2

software was used for image editing. Fluorescence and bright-field images were acquired using an upright motorized microscope (Leica DM 4000 B) fitted with the CoolSnap CF Color camera (Photometrics) and the Micro-Manager software, using the objectives 10× HC PL FLUOTAR (NA 0.30) and 20× HCX PL S-APO (NA 0.50). The Fiji software was used for image editing (Schindelin et al., 2012).

2.17 | Transcriptomic analysis

Total RNA was isolated from PDX-G266 with TRI Reagent (Molecular Research Center, Inc.), and those with RNA Integrity Number > 8 were processed. cDNA libraries were generated from 600-ng RNA using the Stranded mRNA-seq Lib Prep Kit (Illumina), according to the manufacturer's instructions, quantified and checked for quality using capillary electrophoresis. Fifty base pair single-read sequencing was performed on a NextSeq 2000 (Illumina) following the manufacturer's instructions. Reads preprocessing steps were performed using cutadapt 1.10, and reads were mapped onto the hg38 assembly of *Homo sapiens* genome using STAR version 2.5.3a. Gene expression quantification was performed from uniquely aligned reads using htseq-count version 0.6.1p1, with annotations from Ensembl version 108 and 'union' mode. Only non-ambiguously assigned reads were retained for further analyses. Read counts were normalized across libraries by published method (Anders & Huber, 2010). Comparisons of the transcripts was performed on R v4.2.2 by the method (Love et al., 2014) implemented in the DESeq2 Bioconductor library (DESeq2 v1.38.3). Resulting *P*-values were further adjusted for multiple testing. Genes were considered differentially expressed when the adjusted *P*-value was lower than 0.05 and the |log2 Fold-change| > 0.5. Heatmap was performed with pheatmap v1.0.12 and volcano plot with Enhanced-Volcano v1.16.0. Disease Ontology. KEGG and MSigDB annotation was performed using ClusterProlifer v4.6.0 and DOSE v3.24.2 (Yu et al., 2015).

2.18 | Data analysis

The in vitro experiments were not analysed blindly. Data are represented as mean + standard error of the mean (SEM). Data transformation (log) was performed to generate a Gaussian-distributed data set amenable to parametric analysis data. Statistical comparisons were performed using GraphPad Software Prism by Student's *t*-test, one or two-way analysis of variance (ANOVA) followed by a post hoc analysis (Dunnett's or Tukey's post hoc test). Post hoc test was run only when F achieved the necessary level of statistical significance. For statistically significant data, *P*-value was indicated in the figures (GraphPad Software Prism 8). The immuno-related procedures comply with the recommendations made by the *British Journal of Pharmacology* (Alexander et al., 2018). The experimental plan, as well as data and statistical analyses, adheres to the guidelines of the *British Journal of Pharmacology* (Curtis et al., 2022).

2.19 | Nomenclature of targets and ligands

Key protein targets and ligands in this article are hyperlinked to corresponding entries in http://www.guidetopharmacology.org and are permanently archived in the Concise Guide to PHARMACOLOGY 2021/22 (Alexander et al., 2021).

3 | RESULTS

3.1 | Characterization of Xe4Me and Xe4MeCF3 properties

To investigate the impact of Xe4Me and Xe4MeCF3 (Figure 1a) on the 3D structure of the VDR ligand binding domain (LBD), X-ray analyses of the zebrafish VDR LBD in complex with these compounds and a coactivator peptide were performed. The properties of these structures were similar to those of the VDR LBD bound by 1,25D3 or by Xe4 (PDB ID: 2HBH [Rochel et al., 2007]) (Table S1), allowing to compare the paired-contact interaction at a 0.2-Å resolution. The electron density allowed unambiguous fitting of Xe4Me and Xe4MeCF3 into the maps, and the canonical active conformation was similar to the previously reported structures of agonist ligands bound to the VDR LBD (Figure S1A,B). As previously reported for Xe4 (Rochel et al., 2007), the rigidified side chain of Xe4Me and Xe4MeCF3 was straight with ≤1° average deviation from 180° (Figures 1b and S1C). The A-, seco-B- and C/D-rings of Xe4Me and Xe4MeCF3 formed similar interactions with the VDR LBD than those observed with 1,25D3 and Xe4 (Table S2), but differences occurred around the side chains. Indeed, as reported for Xe4, Xe4Me and Xe4MeCF3 did not interact with Leu337 in helix (H)7 (Table S2), a key residue for 1,25D3-induced VDR agonistic conformation (Huet et al., 2015). Moreover, the hydroxy group of C25 from Xe4Me and Xe4MeCF3 formed weaker interactions with His333 and His423 than that from 1,25D3 (Figure S1D and Table S2). However, these weaker interactions were compensated by the entropic gain resulting from the energetically favourable rigid conformation of the ligand, as previously reported for Xe4 (Rochel et al., 2007). Importantly, the addition of the methyl group at C17 allowed Xe4Me and Xe4MeCF3 to form new interactions with Val328 in H6 and Leu341 in H7 (Figure 1c and Table S2). Moreover, the trifluoromethyls led to more or shorter interactions with amino acids in the ligand binding pocket of VDR, notably with Leu440, Val444 and Phe448 (H12); His423 and Tyr427 (H10); Ala331 (H6); and Leu255, Leu258, Ala259 and Val262 (H3) (Figure 1c and Table S2). These results were confirmed by MD analysis of the VDR-Xe4MeCF3 complex showing that the ligand forms stronger interactions with C-terminal residues (Figure S1E) leading to a higher binding affinity, as indicated by the lower calculated binding free energy of the Xe4MeCF3/VDR complex compared with the 1,25D3/VDR complex (Figure S1F). Thus, Xe4MeCF3 is more efficient than 1,25D3, Xe4 and Xe4Me to stabilize the VDR agonistic conformation.

The consequences of the ligand-induced structural modifications of VDR on its interaction with the co-activator SRC1/NCoA1 were

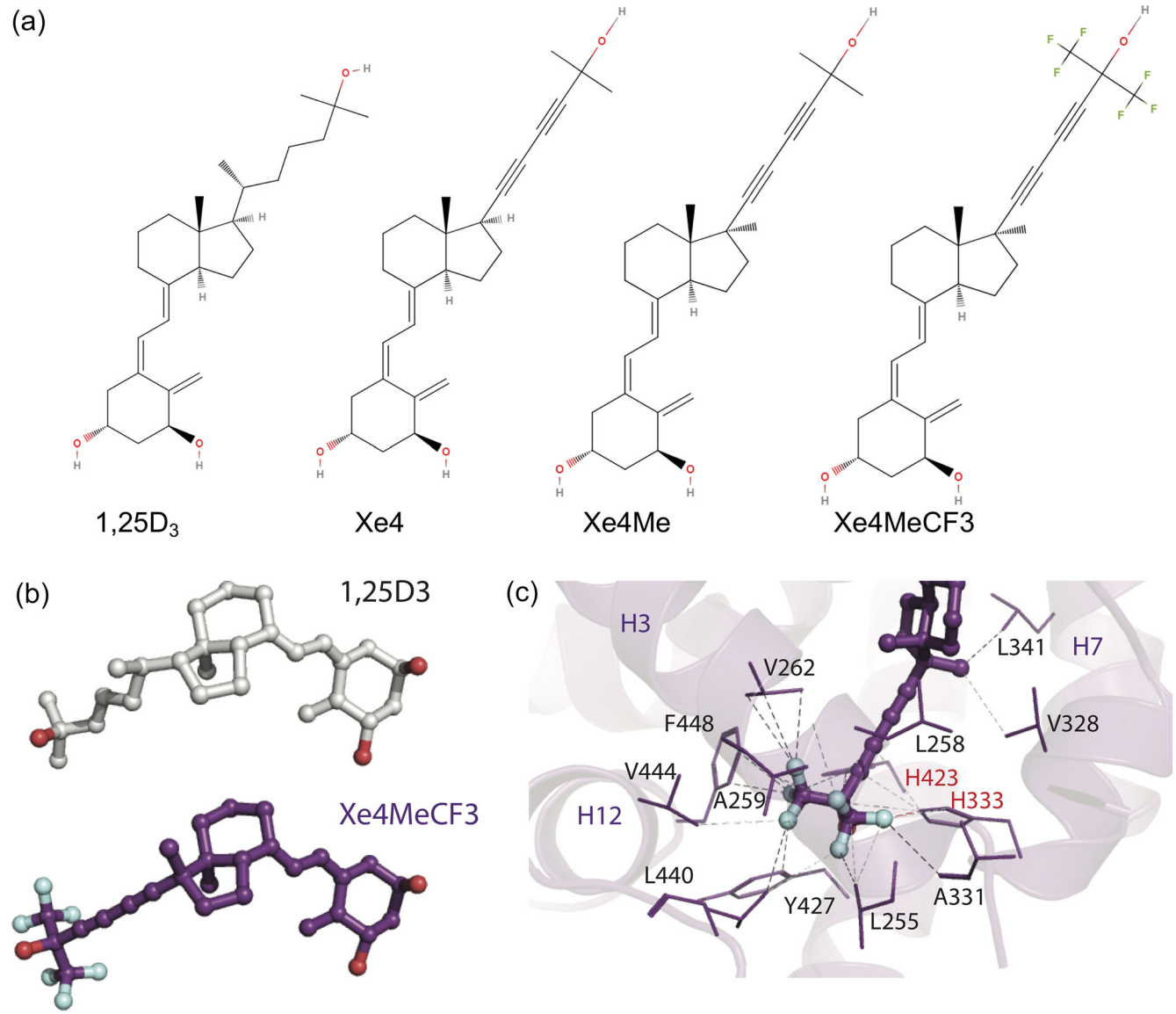

FIGURE 1 Structure of vitamin D receptor (VDR) ligands and characterization of their binding properties. (a) Chemical structure of the VDR ligands used in the study. (b) Conformation of 1,25D3 and Xe4MeCF3 when bound to the zebrafish VDR LBD. (c) Close-up view of the VDR ligand-binding pocket around the Xe4MeCF3 side chain. Residues that contact the ligand with a cutoff of 4.0 Å are labelled. Residues forming van der Waals interaction are depicted in red.

analysed by mammalian two hybrid assays in COS7 cells. Whereas 10-nM 1,25D3 was required to promote the VDR-SRC1 interaction, a similar effect was achieved by Xe4Me at 0.1 nM and by Xe4MeCF3 at 0.001 nM (Figure S2A). Then, the potency of Xe4MeCF3 to induce VDR transcriptional activities was determined by the analysis of the activity of a luciferase reporter under the control of the VDR target gene **CYP24A1** promoter region in HEK 293 EBNA cells transiently transfected with a human (h) VDR expression vector. The maximal luciferase activity was achieved in the presence of 10-nM 1,25D3 as previously described (Belorusova et al., 2022), whereas a 10,000-times lower concentration of Xe4MeCF3 (0.001 nM) was sufficient to reach it (Figure S2B). Thus, a vitamin D analogue with a dyine locked side chain bearing a methyl group at C17, as well as C26 and C27 trifluoromethyls, markedly induced VDR transcriptional activities.

3.2 | Anti-proliferative and pro-calcaemic activities of Xe4MeCF3

MCF7 cells, derived from a pleural effusion of a patient with hormone-sensitive breast carcinoma, are a model classically used to compare anti-cancer activities of VDR agonists (Vanhevel et al., 2022). As previously described (Li et al., 1999), VDR levels were increased in a dose dependent manner in cells treated for 72 h with 1,25D3 compared with vehicle and were even further increased by Xe4MeCF3 treatments (Figure 2a,b). The effects of Xe4MeCF3 on MCF7 cell proliferation were quantified by BrdU incorporation assay. The proliferation of cells treated with 100-nM 1,25D3 or Xe4MeCF3 for 72 h was reduced by 65% compared with vehicle-treated cells (Figure 2c). Importantly, Xe4MeCF3, but not 1,25D3, decreased

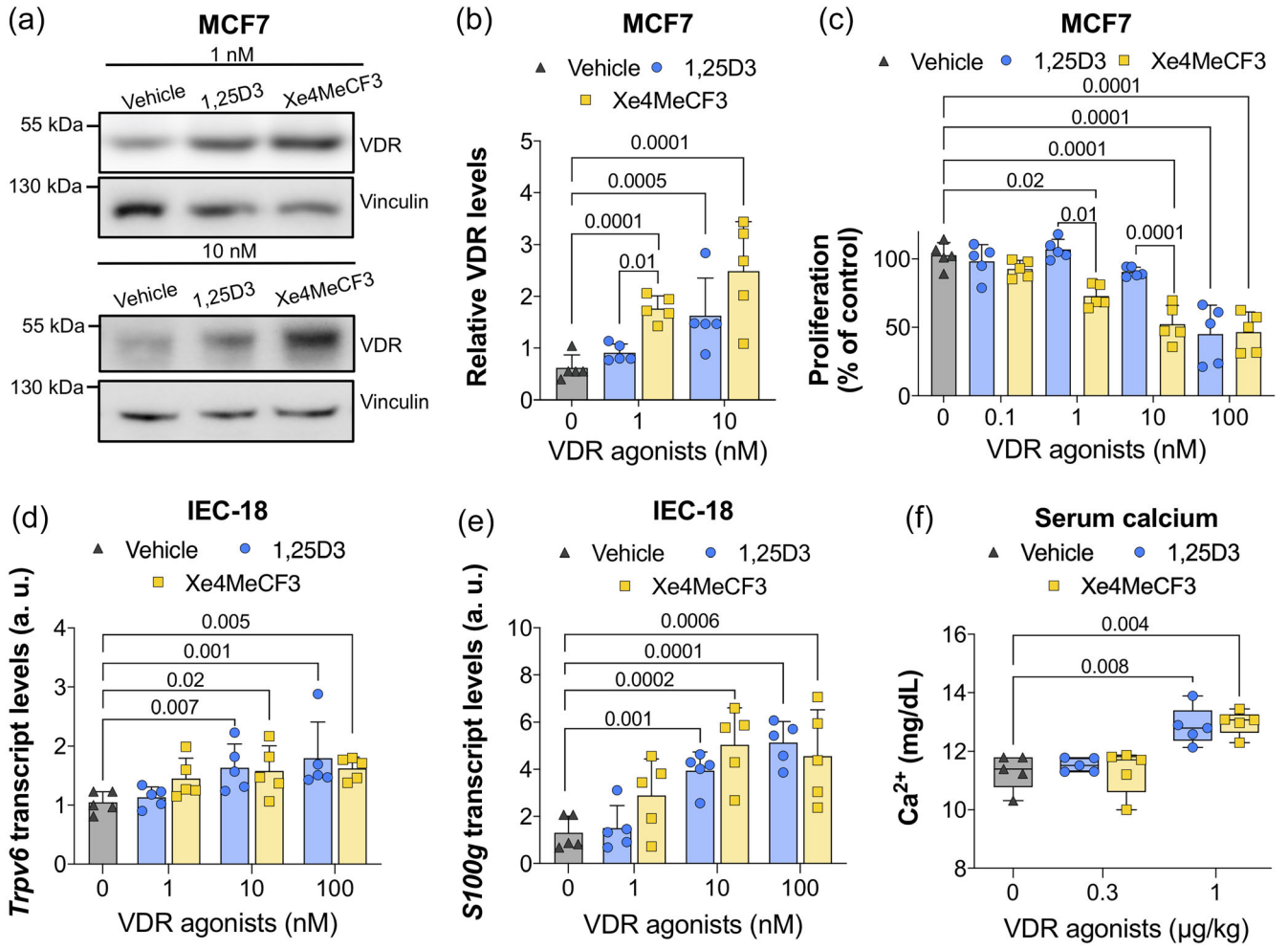

FIGURE 2 Anti-proliferative and pro-calcaemic activities of Xe4MeCF3. Representative vitamin D receptor (VDR) and vinculin immunoblots (a) and fold-change of VDR/vinculin levels (b) determined in total extracts of MCF7 cells treated for 72 h with vehicle (ethanol), 1,25D3 or Xe4MeCF3 at the indicated doses. Vinculin was used as a loading control. n = 5 biological replicates. (c) Cell proliferation rates determined by BrdU incorporation in MCF7 cells treated for 72 h with vehicle, 1,25D3 or Xe4MeCF3 at the indicated doses. Data are represented as percentage of vehicle-treated cells (ethanol). n = 5 biological replicates. *Trpv6* (d) and *S100g* (e) relative transcript levels determined by reverse transcription-quantitative polymerase chain reaction (RT-qPCR) in IEC-18 cells treated for 24 h with vehicle (ethanol), 1,25D3 or Xe4MeCF3 at the indicated doses. n = 5 biological replicates. (f) Calcium levels determined in serum of wild type mice treated for 4 days with vehicle (oil), 0.3 or 1 µg·kg^{-1}·day^{-1} of 1,25D3 or Xe4MeCF3. n = 5 mice/condition; two-way analysis of variance (ANOVA) with Tukey's post hoc test.

MCF7 cell proliferation by 55% at 10 nM and by 35% at 1 nM (Figure 2c). Thus, Xe4MeCF3 increases VDR levels and exerts anti-proliferative activities in hormone-sensitive breast cancer cells at 100-times lower doses than 1,25D3. Note that in immortalized DU 145 cells, obtained from a metastasis of a castration resistant prostate cancer (CRPC) patient, both compounds induced VDR protein levels at 10 and 1 nM, with Xe4MeCF3 inducing higher levels than 1,25D3 at 1 nM (Figure S3A-B). However, even at 100 nM, none of the compounds affected DU-145 cell proliferation (Figure S3C). Thus, Xe4MeCF3 has higher anti-proliferative activities than 1,25D3 on vitamin D sensitive cancer cells.

Because increased intestinal calcium absorption induced by VDR agonists leads to hypercalcaemia, the effects of Xe4MeCF3 were determined in rat intestinal epithelial (IEC-18) cells treated for 24 h. The transcript levels of ***Trpv6*** and *S100g*, two VDR target genes playing key roles in calcium homeostasis (Christakos et al., 2016), were similar in IEC-18 cells treated with 1-nM 1,25D3, 1-nM Xe4MeCF3 and vehicle (Figure 2d,e). In contrast, 10 and 100 nM of 1,25D3 or Xe4MeCF3 induced *Trpv6* transcripts by 1.5-fold and *S100g* transcripts by four-fold compared with vehicle-treated IEC-18 cells (Figure 2d,e). To determine the effects of Xe4MeCF3 on calcium homeostasis in vivo, wild-type mice were treated *per os* for 4 consecutive days. Serum calcium levels were similar in mice treated with vehicle, 0.3 µg·kg^{-1}·day^{-1} of 1,25D3 or 0.3 µg·kg^{-1}·day^{-1} of Xe4MeCF3. In contrast, treatments with 1 µg·kg^{-1}·day^{-1} induced hypercalcaemia in both 1,25D3 and Xe4MeCF3 treated mice (Figure 2f). Thus, Xe4MeCF3's pro-calcaemic activity is similar to that of 1,25D3. Altogether, these results demonstrate that Xe4MeCF3 has anti-proliferative effects in cancer cells at lower doses than the natural ligand but similar pro-calcaemic activities in intestinal cells. Thus, the cell-specific activities of Xe4MeCF3 might confer to this VDR agonist a wider therapeutic index in vivo.

3.3 | Effects of VDR agonists and docetaxel combination in PCa spheroids

To investigate the effects of VDR agonists on primary PCa cells, immortalized IGR-CaP1 cells (Chauchereau et al., 2011) and their docetaxel-resistant derivate IGR-CaP1-R100 (Al Nakouzi et al., 2014) were utilized. Note that both cell lines are **AR** negative (Al Nakouzi et al., 2014; Chauchereau et al., 2011). VDR immunoblotting of IGR-CaP1 and IGR-CaP1-R100 extracts demonstrated that VDR levels were 5 times higher in the presence of 10-nM 1,25D3 or Xe4MeCF3 (Figure S4A,B), indicating that these cells are responsive to VDR agonists. Because cancer cell lines cultured in 3D are more appropriate to investigate the response of tumour cells to chemotherapy than cells cultured in a monolayer (Jubelin et al., 2022), we analysed the effects

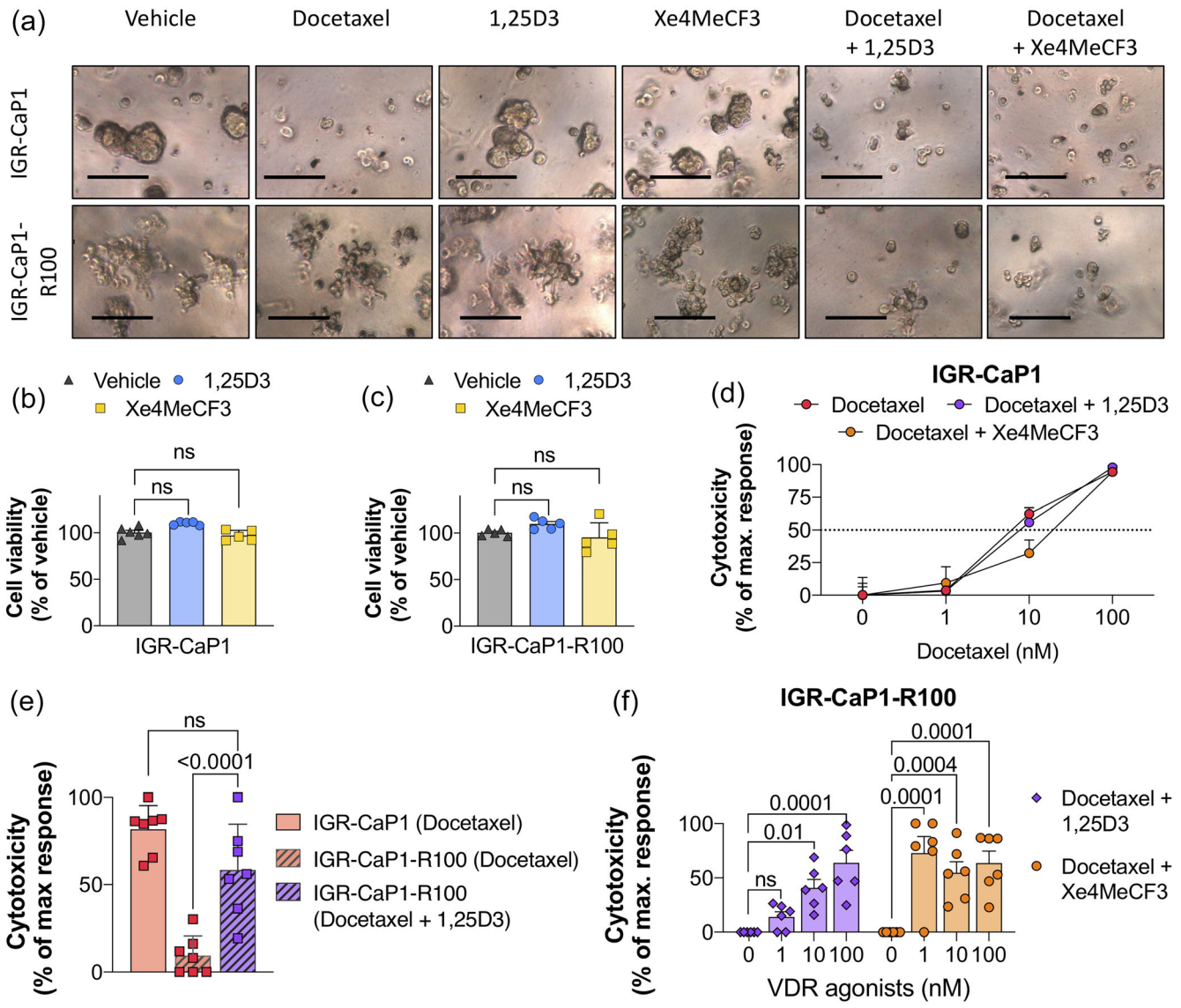

FIGURE 3 Vitamin D receptor (VDR) agonists and docetaxel effects in prostate cancer (PCa) spheroids. (a) Representative images of IGR-CaP1 and IGR-CaP1-R100 spheroids, treated for 72 h with vehicle, 100 nM docetaxel, 100-nM 1,25D3 or 100-nM Xe4MeCF3 alone or in combination. Scale bar = 150 µm. n = 5 biological replicates. Cell viability in IGR-CaP1 (b) and IGR-CaP1-R100 (c) spheroids treated for 72 h with 100-nM 1,25D3, 100-nM Xe4MeCF3 or vehicle (ethanol), represented as percentage of vehicle-treated cells. n = 5 biological replicates. ns, $P \geq 0.05$; one-way analysis of variance (ANOVA). (d) Cytotoxicity in IGR-CaP1 spheroids treated for 72 h with docetaxel at the indicated doses in the presence or absence of 100-nM 1,25D3 or 100 nM Xe4MeCF3, normalized to the corresponding condition in the absence of docetaxel and represented as percentage of maximal response. n = 7 biological replicates. Not indicated, $P \geq 0.05$; two-way ANOVA. (e) Cytotoxicity in IGR-CaP1 spheroids treated for 72 h with 100-nM docetaxel and in IGR-CaP1-R100 spheroids treated for 72 h with 100-nM docetaxel in the presence or absence of 100-nM 1,25D3, normalized to the corresponding condition in the absence of docetaxel and represented as percentage of maximal response. n = 7 biological replicates. One-way ANOVA with Dunnett's post hoc. ns, $P \geq 0.05$. (f) Cytotoxicity in IGR-CaP1-R100 spheroids treated for 72 h with 100-nM docetaxel in the presence or absence of 1, 10 or 100 nM of 1,25D3 or Xe4MeCF3, normalized to the corresponding condition in the absence of docetaxel, and represented as percentage of maximal response. n = 6 biological replicates. ns, $P \geq 0.05$; two-way ANOVA with Tukey's post hoc test.

of VDR agonists and docetaxel in IGR-CaP1 and IGR-CaP1-R100 spheroids. The area of IGR-CaP1 spheroids was reduced by 50% in the presence of 100-nM docetaxel, whereas that of IGR-CaP1-R100 spheroids was unaffected (Figures 3a and S5A,B). In addition, IGR-CaP1-R100 spheroids were resistant to higher doses of docetaxel than IGR-CaP1 spheroids in cell viability tests assessed by CellTiter-Glo (Figure S5C). Thus, IGR-CaP1 spheroids exhibit signs of docetaxel cytotoxicity, whereas those of IGR-CaP1-R100 are resistant. The treatments with 100-nM 1,25D3 or Xe4MeCF3 for 72 h had no cytotoxic effect in IGR-CaP1 and IGR-CaP1-R100 spheroids (Figure 3a–c and S5A,B), and these treatments did not enhance the cytotoxic effect of docetaxel in IGR-CaP1 spheroids (Figures 3a,d and S5A). Importantly, whereas 100-nM docetaxel had no effect on IGR-CaP1-R100 spheroids, the co-treatment with docetaxel and 100-nM 1,25D3 induced a cytotoxicity similar to that observed in IGR-CaP1 spheroids (Figures 3a,e and S5B). In addition, the area of IGR-CaP1-R100 spheroids co-treated with 1,25D3 and docetaxel was reduced (Figure 3a and S5A,B), indicating that such a co-treatment reduces the cell number. Xe4MeCF3 and 1,25D3 restored docetaxel cytotoxicity in IGR-CaP1-R100 spheroids at 100 and 10 nM, whereas only Xe4MeCF3 was efficient at 1 nM (Figure 3a,f). The Loewe method was used to determine the drug CI in IGR-CaP1-R100 spheroids (Ianevski et al., 2020). Whereas no synergistic effect was shown at 10-nM docetaxel, both 1,25D3 and Xe4MeCF3 have synergistic effects with 50-, 100- and 200-nM docetaxel (Figure S5D,E). Moreover, this synergy was reached by Xe4MeCF3 at a dose 10-times lower than that of 1,25D3 (Figure S5E). Thus, VDR agonists induce docetaxel cytotoxicity in chemoresistant PCa cell lines, and Xe4MeCF3 is more potent than 1,25D3.

3.4 | Effects of Xe4MeCF3 and docetaxel co-treatment in xenografts derived from a patient with chemoresistant CRPC

Because the efficacy of docetaxel chemotherapy for CRPC is limited by the development of resistance (Galsky & Vogelzang, 2010), Xe4MeCF3 effects alone or in combination with docetaxel were

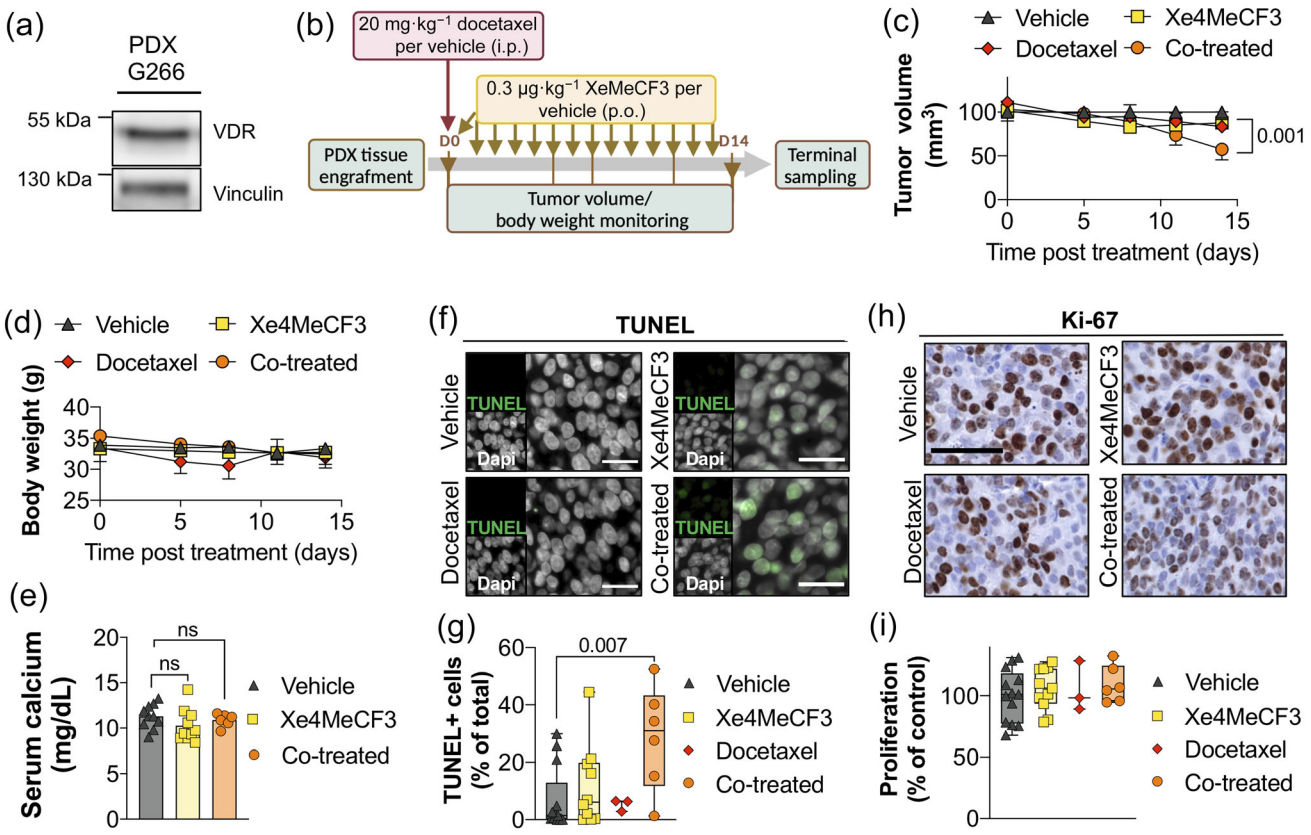

FIGURE 4 Effects of vitamin D receptor (VDR) agonists and docetaxel on PDX-G266. (a) Representative VDR and vinculin immunoblot in total extracts of PDX-G266. n = 10 mice. (b) Schematic representation of the experimental protocol: i.p., intra-peritoneal; p.o., *per os*. (c) Tumour growth monitoring (mm^3) in PDX-G266 mice for 14 days. n = 13 vehicle, n = 10 Xe4MeCF3, n = 3 docetaxel, n = 7 co-treated mice; two-way analysis of variance (ANOVA) with Tukey's post hoc test. (d) Body weight of PDX-G266 mice treated for 14 days as indicated. n = 13 vehicle, n = 10 Xe4MeCF3, n = 3 docetaxel, n = 7 co-treated; two-way ANOVA. (e) Calcium levels determined in serum of PDX-G266 mice treated as indicated. n = 6 co-treated, n = 10 vehicle/Xe4MeCF3-treated mice, ns, $P \geq 0.05$, one-way ANOVA. Representative images (f) and quantification (g) of cell death determined by TUNEL assay on sections from PDX-G266. TUNEL/fluorescein (green) and DAPI (grey). Scale bar, 20 µm. n = 13 vehicle, n = 10 Xe4MeCF3, n = 3 docetaxel, n = 6 co-treated. Representative immunostaining (h) and quantification (i) of Ki-67 on PDX-G266 sections. Scale bar = 50 µm. n = 13 vehicle, n = 10 Xe4MeCF3, n = 3 docetaxel, n = 6 co-treated. Not indicated, $P \geq 0.05$.

investigated on a patient-derived xenograft model (PDX-G266) established from a pelvectomy of a CRPC patient, a non-responder to the second-line hormone therapy **enzalutamide** (Béraud et al., 2023), that expresses VDR (Figure 4a). PDX-G266 was defined as a CRPC model with AR+ status due to a missense AR activating mutation (Béraud et al., 2023). The tumour growth was not affected up to 24 days after a single administration of docetaxel (Figure S6A,B) (Béraud et al., 2023). In accordance with the previous results, the histological

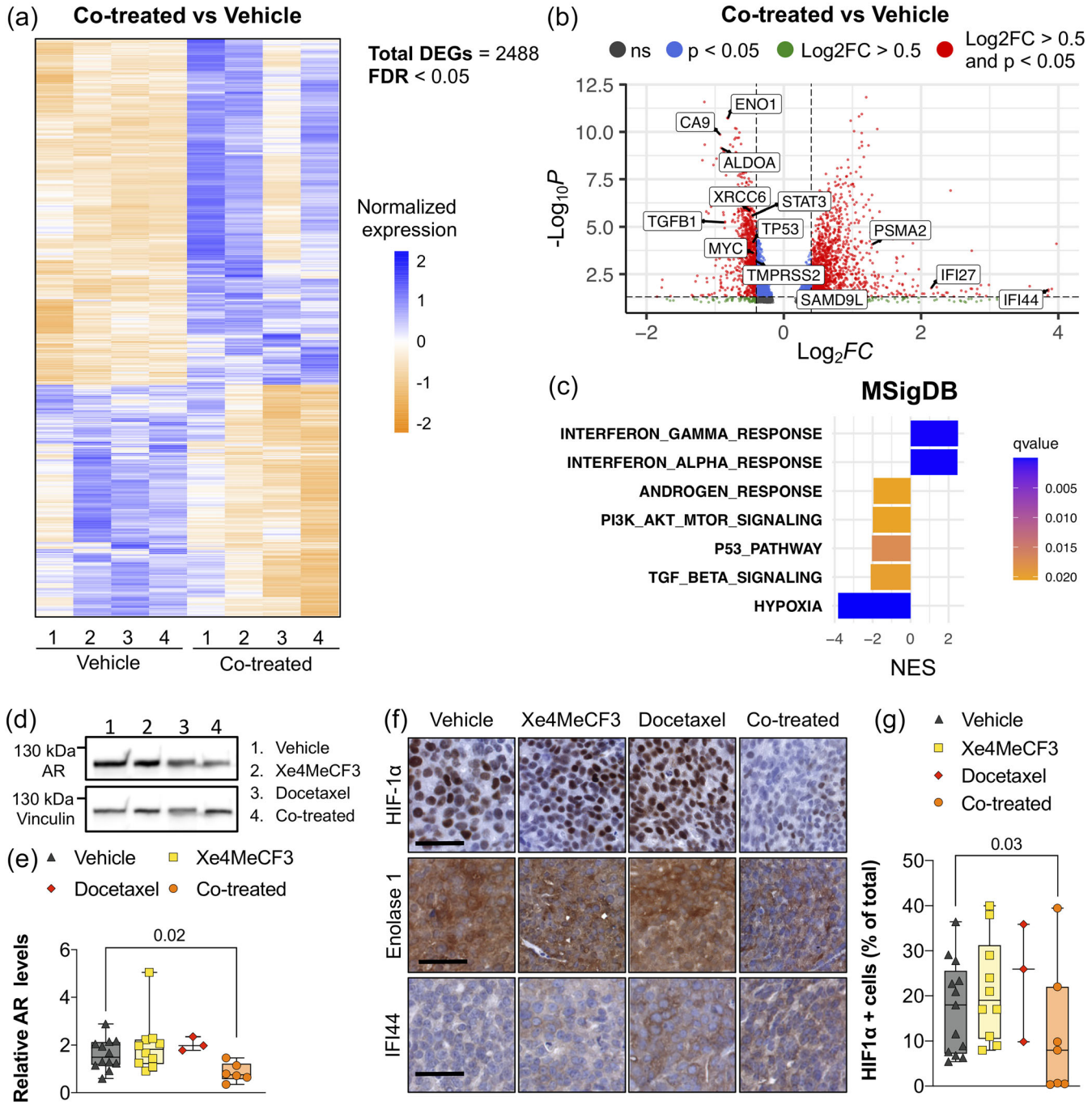

FIGURE 5 Molecular pathways in remaining tumour cells of co-treated PDX-G266 mice. (a) Heatmap of down- (orange) and up-regulated (blue) differentially expressed genes (DEGs) between co-treated and vehicle-treated PDX-G266 mice. (b) Volcano plot of DEGs between co-treated and vehicle-treated PDX-G266 mice. ns, $P \geq 0.05$. (c) DEGs annotation using Molecular Signatures Database (MSigDB). NES: normalized enriched score. Representative AR and vinculin immunoblots (d) and average fold-change (e) in total extracts of PDX-G266. n = 13 vehicle, n = 10 Xe4MeCF3, n = 3 docetaxel, n = 6 co-treated; one-way analysis of variance (ANOVA) with Dunnett's post hoc. Vinculin was used as a loading control. (f) Representative immunostaining of HIF-1α, enolase 1 and IFI44 on PDX-G266 sections from mice treated for 14 days as indicated. Scale bar = 50 µm. n = 13 vehicle, n = 10 Xe4MeCF3, n = 3 docetaxel, n = 7 co-treated. (g) Quantification of HIF-1α positive cells on PDX-G266 sections. n = 13 vehicle, n = 10 Xe4MeCF3, n = 3 docetaxel, n = 7 co-treated. One-way ANOVA with Dunnett's post hoc. Not indicated, $P \geq 0.05$.

analysis of these tumours showed that the proportion of PDX-G266 proliferating cells, determined by Ki67 immunostaining, is similar between docetaxel- and vehicle-treated groups (Figure S6C,D). In addition, no apoptotic cells were identified by TUNEL assay or cleaved **caspase 3** immunostaining (Figure S6E–G). Thus, PDX-G266 is a docetaxel-resistant mouse model.

The effect of Xe4MeCF3 at the highest dose that does not induce hypercalcaemia (Figure 2f), namely, 0.3 $\mu g \cdot kg^{-1} \cdot day^{-1}$, was investigated (Figure 4b). Consistent with the results obtained in IGR-CaP1-R100 spheroids, a daily treatment with Xe4MeCF3 for 14 days did not induce tumour growth inhibition (Figure 4c). Then, the effects of a combinatory regimen based on a single administration of docetaxel and 0.3 $\mu g \cdot kg^{-1} \cdot day^{-1}$ Xe4MeCF3 (termed co-treatment) were investigated (Figure 4b). Despite similar body weight in the co-treated mice, and in the docetaxel-, Xe4MeCF3- or vehicle-treated ones (Figure 4d), three co-treated mice were removed from the study due to side effects of the chemotherapy (e.g. diarrhoea). Importantly, the tumour volume in co-treated PDX-G266 mice was twice smaller than in vehicle- or single therapy (docetaxel or Xe4MeCF3)-treated mice (Figure 4c). Of note, serum calcium levels were similar in vehicle-, Xe4MeCF3- or co-treated PDX-G266 mice (Figure 4e). Moreover, the number of TUNEL-positive cells was enhanced in tumours from the co-treated group compared with those from the groups treated with a single therapy or with vehicle (Figure 4f,g), showing a cytotoxic effect of the co-treatment. Thus, a docetaxel and XeMeCF3 co-treatment induces apoptosis and reduces tumour growth without inducing hypercalcaemia in docetaxel-resistant PDX-G266 tumours.

Tumour relapse is often limiting current PCa clinical care. To characterize the pro-tumoral potency of the remaining tumour cells, histological analysis was performed by H&E staining at Day 14 and showed a similar PDX-G266 tumour architecture in the different cohorts (Figure S7). A similar number of Ki-67-positive cells was observed in the various groups (Figure 4h,i). To characterize the molecular features in the remaining cells at Day 14, the transcriptome of the xenografts from 4 co-treated and 4 vehicle-treated PDX-G266 mice was compared, and 2488 differentially expressed genes (DEGs), including 995 down-regulated and 1493 up-regulated, were identified (Figure 5a,b and Table S3). Molecular signature database (MSigDB) and Kyoto Encyclopedia of Genes and Genomes (KEGG) analysis revealed that the top ranked pathways of the down-regulated DEGs are associated with androgen (i.e. ***TMPRSS2*** and ***NDRG1***), tumour protein p53 (i.e. *TP53* and *PIDD1*), mechanistic target of rapamycin (i.e. ***TRIB3***, ***EGFR***, *MCM2* and ***MTOR***), transforming growth factor beta 1 (i.e. ***ENG***, ***HIPK2***, ***THBS1*** and ***TGFB1***) and hypoxia (i.e. *ENO1*, *ALDOA1* and ***CA9***) signalling, and the up-regulated transcripts were closely associated with interferon-α and γ signalling (i.e. *IFI44*, *IFIT3*, *PSMA2* and *SAMD9L*) (Figure 5b,c and Tables S4 and S5). Because transcriptomic data revealed that the androgen response is down-regulated in co-treated tumours, the effect of the combined treatment on AR levels was analysed by immunoblotting and showed that they were twice lower in co-treated mice than in those treated with Xe4MeCF3, docetaxel or vehicle (Figure 5d,e). Because transcripts related to hypoxia also were down-regulated, the levels of hypoxia inducible factor 1A (HIF-1α) were quantified by immunostaining. The protein levels of HIF-1α were 5-times lower, and those of its target gene *Enolase 1* reduced in the co-treated group compared to Xe4MeCF3, docetaxel and vehicle-treated mice (Figure 5f,g). Moreover, and in agreement with the transcriptomic data (Figure 5b), immunostaining revealed an increase of interferon induced protein 44 (IFI44) protein levels in Xe4MeCF3-, docetaxel- or co-treated mice compared with those treated with vehicle (Figure 5e). Of note, the percentage of HIF-1α+ cells and the levels of Enolase 1 or IFI44 were similar to those of vehicle-treated mice 24 days post docetaxel administration (Figure S6G,H), demonstrating that docetaxel alone has no effect on these pathways. Thus, in addition of a reduced tumour size, pathways playing key role in prostatic carcinoma progression were reduced by the co-treatment in the remaining cells. Altogether, the combination of Xe4MeCF3 with docetaxel has cytotoxic effects on chemoresistant CRPC patient derived xenografts and down-regulates pathways associated with cancer aggressiveness in the remaining cells.

4 | DISCUSSION AND CONCLUSIONS

In the present work, we demonstrate that docetaxel resistance in PCa is overcome by co-treatment with VDR agonists, opening new avenues for vitamin D-based therapeutic strategies for advanced PCa.

VDR is expressed in almost every cell type and has pleiotropic effects in several cancers (Feldman et al., 2014). The pro-calcaemic and anti-proliferative activities of 1,25D3-bound VDR are achieved at similar doses, resulting in important safety issues. To circumvent this limitation, we characterized the biological activities of structure-based improved 1,25D3 analogues bearing several chemical modifications, comprising a rigid side chain, an additional methyl group at position C17 and geminal trifluoromethyl groups. By comparing Xe4, Xe4Me and Xe4MeCF3, we unravelled that the latter is the most potent ligand. Xe4MeCF3 exhibits an energetically favourable conformation and increases the stability of the complex by additional van der Waals interaction contacts of the C-17 methyl and fluorine atoms. Compared with several closely-related analogues for which the crystal structures were solved and the transactivation potencies characterized (Belorusova & Rochel, 2016), Xe4MeCF3 stabilizes the active conformation of the VDR LBD that is essential for its biological activities. Importantly, whereas Xe4MeCF3 affects serum calcium levels at similar doses than 1,25D3, it exerts antiproliferative activities at lower doses in vitro. Therefore, Xe4MeCF3 represents a powerful tool to decipher the potency of VDR agonists in vivo.

Development of chemoresistance represents the main limitation of the clinical care of advanced PCa (Galsky & Vogelzang, 2010). Even though **cabazitaxel** improves the overall survival of patients with docetaxel-resistant CRPC, its use in clinical practice is limited by important adverse effects (Yanagisawa et al., 2023). Numerous epidemiological and preclinical studies supported the use of VDR agonists as a single-agent therapy for PCa, but the poor consistency of the clinical data has contributed to dampen the enthusiasm for such

therapeutic options (Trump & Aragon-Ching, 2018). In line with these results, we show that VDR agonists have no effect on spheroids derived from PCa with an AR− status. In contrast, we demonstrate that VDR agonists in combination with docetaxel exert cytotoxic effects on chemoresistant spheroids, showing that vitamin D-based therapies represent a promising option to overcome drug-resistances.

Even though the results of the clinical trials investigating the potency of 1,25D3 and docetaxel combination in CRPC patients were encouraging, their design (hypercalcaemic doses or low doses) strongly compromised the outcome (Trump, 2018; Trump & Aragon-Ching, 2018). To confirm our in vitro findings in an independent patient-derived cell line and challenge our hypothesis, we utilized a patient derived xenograft model of docetaxel-resistant CRPC. This mouse model recapitulates the characteristic of the tumour of origin and represents a powerful tool to study the potency of new therapeutic strategies (Béraud et al., 2023). These mice were treated with 0.3 $\mu g \cdot kg^{-1} \cdot day^{-1}$ Xe4MeCF3, a normocalcaemic regimen that was about 4-times higher than that of 1,25D3 used in the ASCENT trial. In line with the results obtained in vitro, where single agent therapy had no therapeutic effects, the combination of Xe4MeCF3 and docetaxel reduced tumour growth. In addition, transcriptomic analysis coupled to its validation by immunohistostaining showed that the co-treatment down-regulates pathways associated with PCa progression in the remaining cells.

Taken together, this work demonstrates that VDR agonists and docetaxel combined therapies represent a promising strategy to reduce chemoresistant PCa progression, which required further clinical investigation.

AUTHOR CONTRIBUTIONS

K. Len: Conceptualization (lead); validation (lead); formal analysis (lead); investigation (lead); data curation; visualization (lead); writing—original draft (lead); writing—review & editing (lead). **C. Beraud:** Methodology; formal analysis; investigation (equal); resources (equal). **C. Fauveau:** Methodology; validation (equal); formal analysis (equal); investigation (equal). **A.Y. Belorusova:** Methodology; formal analysis; investigation (equal). **Y. Chebaro:** Validation (equal); formal analysis (equal); investigation (equal). **A. Mourino:** Resources (equal). **T. Massfelder:** Methodology; resources (equal). **Anne Chauchereau:** resources (equal). **D. Metzger:** Writing—original draft (equal); writing—review & editing (equal); supervision (equal); funding acquisition (equal). **N. Rochel:** Data curation (equal); writing—original draft (equal); writing—review & editing (equal); supervision (equal); funding acquisition (equal). **G. Laverny:** Conceptualization (lead); methodology (equal); formal analysis (equal); data curation (equal); writing—original draft (lead); writing—review & editing (lead); supervision (lead); project administration (lead); funding acquisition (lead).

ACKNOWLEDGEMENTS

We thank the IGBMC animal facility, cell culture and histology services. We acknowledge the support of the Light Microscopy Facility at the IGBMC imaging centre, member of the national infrastructure France-BioImaging supported by the French National Research Agency (ANR-10-INBS-04), as well as that of GenomEast, a member of the 'France Génomique' consortium (ANR-10-INBS-0009). We thank L. Ramspacher for her contribution and Hinrich Gronemeyer (IGBMC) for providing the Gal4 DBD-NCoA1 construct.

CONFLICT OF INTEREST STATEMENT

The authors declare that they have no conflict of interest.

DATA AVAILABILITY STATEMENT

Atomic coordinates and related structure factors have been deposited in the Protein Data Bank with accession codes: 8P9X (VDR-Xe4Me) and 8P9W (VDR-Xe4MeCF3). RNA sequencing raw data are available in GEO database (GSE 241426).

DECLARATION OF TRANSPARENCY AND SCIENTIFIC RIGOUR

This declaration acknowledges that this paper adheres to the principles for transparent reporting and scientific rigour of preclinical research as stated in the BJP guidelines for Design and Analysis, Immunoblotting and Immunochemistry and Animal Experimentation and as recommended by funding agencies, publishers and other organizations engaged with supporting research.

ORCID

Kateryna Len-Tayon https://orcid.org/0000-0002-5397-391X

Gilles Laverny https://orcid.org/0000-0002-2666-6877

REFERENCES

Adams, P. D., Afonine, P. V., Bunkóczi, G., Chen, V. B., Davis, I. W., Echols, N., Headd, J. J., Hung, L. W., Kapral, G. J., Grosse-Kunstleve, R. W., McCoy, A. J., Moriarty, N. W., Oeffner, R., Read, R. J., Richardson, D. C., Richardson, J. S., Terwilliger, T. C., & Zwart, P. H. (2010). *PHENIX*: A comprehensive python-based system for macromolecular structure solution. *Acta Crystallographica. Section D, Biological Crystallography*, *66*, 213–221. https://doi.org/10.1107/S0907444909052925

al Nakouzi, N., Cotteret, S., Commo, F., Gaudin, C., Rajpar, S., Dessen, P., Vielh, P., Fizazi, K., & Chauchereau, A. (2014). Targeting CDC25C, PLK1 and CHEK1 to overcome docetaxel resistance induced by loss of LZTS1 in prostate cancer. *Oncotarget*, *5*, 667–678. https://doi.org/10.18632/oncotarget.1574

Alexander, S. P. H., Kelly, E., Mathie, A., Peters, J. A., Veale, E. L., Armstrong, J. F., Faccenda, E., Harding, S. D., Pawson, A. J., Southan, C., Davies, J. A., Amarosi, L., Anderson, C. M. H., Beart, P. M., Broer, S., Dawson, P. A., Hagenbuch, B., Hammond, J. R., Hancox, J. C., … Verri, T. (2021). The concise guide to pharmacology 2021/22: Transporters. *British Journal of Pharmacology*, *178*, S412-S513. https://doi.org/10.1111/bph.15543

Alexander, S. P. H., Roberts, R. E., Broughton, B. R. S., Sobey, C. G., George, C. H., Stanford, S. C., Cirino, G., Docherty, J. R., Giembycz, M. A., Hoyer, D., Insel, P. A., Izzo, A. A., Ji, Y., MacEwan, D. J., Mangum, J., Wonnacott, S., & Ahluwalia, A. (2018). Goals and practicalities of immunoblotting and immunohistochemistry: A guide for submission to the British Journal of Pharmacology. *British Journal of Pharmacology*, *175*, 407–411. https://doi.org/10.1111/bph.14112

Anders, S., & Huber, W. (2010). Differential expression analysis for sequence count data. *Genome Biology*, *11*, R106. https://doi.org/10.1186/gb-2010-11-10-r106

Attia, Y. M., el-Kersh, D. M., Ammar, R. A., Adel, A., Khalil, A., Walid, H., Eskander, K., Hamdy, M., Reda, N., Mohsen, N. E., al-Toukhy, G. M.,

Mansour, M. T., & Elmazar, M. M. (2020). Inhibition of aldehyde dehydrogenase-1 and p-glycoprotein-mediated multidrug resistance by curcumin and vitamin D3 increases sensitivity to paclitaxel in breast cancer. *Chemico-Biological Interactions*, *315*, 108865. https://doi.org/10.1016/j.cbi.2019.108865

Beer, T. M. (2005). ASCENT: The androgen-independent prostate cancer study of calcitriol enhancing taxotere. *BJU International*, *96*, 508–513. https://doi.org/10.1111/j.1464-410X.2005.05675.x

Belorusova, A. Y., & Rochel, N. (2016). Structural studies of vitamin D nuclear receptor ligand-binding properties. In *Vitamins & Hormones* (pp. 83–116). Elsevier.

Belorusova, A. Y., Rovito, D., Chebaro, Y., Doms, S., Verlinden, L., Verstuyf, A., Metzger, D., Rochel, N., & Laverny, G. (2022). Vitamin D analogs bearing C-20 modifications stabilize the agonistic conformation of non-responsive vitamin D receptor variants. *IJMS*, *23*, 8445. https://doi.org/10.3390/ijms23158445

Béraud, C., Bidan, N., Lassalle, M., Lang, H., Lindner, V., Krucker, C., Masliah-Planchon, J., Potiron, E., Lluel, P., Massfelder, T., Allory, Y., & Misseri, Y. (2023). A new tumorgraft panel to accelerate precision medicine in prostate cancer. *Frontiers in Oncology*, *13*, 1130048. https://doi.org/10.3389/fonc.2023.1130048

Bikle, D., & Christakos, S. (2020). New aspects of vitamin D metabolism and action—Addressing the skin as source and target. *Nature Reviews. Endocrinology*, *16*, 234–252. https://doi.org/10.1038/s41574-019-0312-5

Chauchereau, A., al Nakouzi, N., Gaudin, C., le Moulec, S., Compagno, D., Auger, N., Bénard, J., Opolon, P., Rozet, F., Validire, P., Fromont, G., & Fizazi, K. (2011). Stemness markers characterize IGR-CaP1, a new cell line derived from primary epithelial prostate cancer. *Experimental Cell Research*, *317*, 262–275. https://doi.org/10.1016/j.yexcr.2010.10.012

Christakos, S., Dhawan, P., Verstuyf, A., Verlinden, L., & Carmeliet, G. (2016). Vitamin D: Metabolism, molecular mechanism of action, and pleiotropic effects. *Physiological Reviews*, *96*, 365–408. https://doi.org/10.1152/physrev.00014.2015

Curtis, M. J., Alexander, S. P. H., Cirino, G., George, C. H., Kendall, D. A., Insel, P. A., Izzo, A. A., Ji, Y., Panettieri, R. A., Patel, H. H., Sobey, C. G., Stanford, S. C., Stanley, P., Stefanska, B., Stephens, G. J., Teixeira, M. M., Vergnolle, N., & Ahluwalia, A. (2022). Planning experiments: Updated guidance on experimental design and analysis and their reporting III. *British Journal of Pharmacology*, *179*, 3907–3913. https://doi.org/10.1111/bph.15868

Eelen, G., Valle, N., Sato, Y., Rochel, N., Verlinden, L., de Clercq, P., Moras, D., Bouillon, R., Muñoz, A., & Verstuyf, A. (2008). Superagonistic fluorinated vitamin D3 analogs stabilize helix 12 of the vitamin D receptor. *Chemistry & Biology*, *15*, 1029–1034. https://doi.org/10.1016/j.chembiol.2008.08.008

Eelen, G., Verlinden, L., Rochel, N., Claessens, F., de Clercq, P., Vandewalle, M., Tocchini-Valentini, G., Moras, D., Bouillon, R., & Verstuyf, A. (2005). Superagonistic action of 14-epi-analogs of 1,25-dihydroxyvitamin D explained by vitamin D receptor-coactivator interaction. *Molecular Pharmacology*, *67*, 1566–1573. https://doi.org/10.1124/mol.104.008730

Emsley, P., & Cowtan, K. (2004). *Coot*: Model-building tools for molecular graphics. *Acta Crystallographica. Section D, Biological Crystallography*, *60*, 2126–2132. https://doi.org/10.1107/S0907444904019158

Evans, P. (2006). Scaling and assessment of data quality. *Acta Crystallographica. Section D, Biological Crystallography*, *62*, 72–82. https://doi.org/10.1107/S0907444905036693

Feldman, D., Krishnan, A. V., Swami, S., Giovannucci, E., & Feldman, B. J. (2014). The role of vitamin D in reducing cancer risk and progression. *Nature Reviews. Cancer*, *14*, 342–357. https://doi.org/10.1038/nrc3691

Galsky, M. D., & Vogelzang, N. J. (2010). Docetaxel-based combination therapy for castration-resistant prostate cancer. *Annals of Oncology*, *21*, 2135–2144. https://doi.org/10.1093/annonc/mdq050

Hershberger, P. A., Yu, W. D., Modzelewski, R. A., Rueger, R. M., Johnson, C. S., & Trump, D. L. (2001). Calcitriol (1,25-dihydroxycholecalciferol) enhances paclitaxel antitumor activity in vitro and in vivo and accelerates paclitaxel-induced apoptosis. *Clinical Cancer Research*, *7*, 1043–1051.

Huang, Z., Zhang, Y., Li, H., Zhou, Y., Zhang, Q., Chen, R., Jin, T., Hu, K., Li, S., Wang, Y., Chen, W., & Huang, Z. (2019). Vitamin D promotes the cisplatin sensitivity of oral squamous cell carcinoma by inhibiting LCN2-modulated NF-κB pathway activation through RPS3. *Cell Death & Disease*, *10*, 936. https://doi.org/10.1038/s41419-019-2177-x

Huet, T., Laverny, G., Ciesielski, F., Molnár, F., Ramamoorthy, T. G., Belorusova, A. Y., Antony, P., Potier, N., Metzger, D., Moras, D., & Rochel, N. (2015). A vitamin D receptor selectively activated by Gemini analogs reveals ligand dependent and independent effects. *Cell Reports*, *10*, 516–526. https://doi.org/10.1016/j.celrep.2014.12.045

Ianevski, A., Giri, A. K., & Aittokallio, T. (2020). SynergyFinder 2.0: Visual analytics of multi-drug combination synergies. *Nucleic Acids Research*, *48*, W488–W493. https://doi.org/10.1093/nar/gkaa216

Jubelin, C., Muñoz-Garcia, J., Griscom, L., Cochonneau, D., Ollivier, E., Heymann, M.-F., Vallette, F. M., Oliver, L., & Heymann, D. (2022). Three-dimensional in vitro culture models in oncology research. *Cell & Bioscience*, *12*, 155. https://doi.org/10.1186/s13578-022-00887-3

Kabsch, W. (2010). XDS. *Acta Crystallographica. Section D, Biological Crystallography*, *66*, 125–132. https://doi.org/10.1107/S0907444909047337

Kollman, P. A., Massova, I., Reyes, C., Kuhn, B., Huo, S., Chong, L., Lee, M., Lee, T., Duan, Y., Wang, W., Donini, O., Cieplak, P., Srinivasan, J., Case, D. A., & Cheatham, T. E. (2000). Calculating structures and free energies of complex molecules: Combining molecular mechanics and continuum models. *Accounts of Chemical Research*, *33*, 889–897. https://doi.org/10.1021/ar000033j

Laverny, G., Penna, G., Uskokovic, M., Marczak, S., Maehr, H., Jankowski, P., Ceailles, C., Vouros, P., Smith, B., Robinson, M., Reddy, G. S., & Adorini, L. (2009). Synthesis and anti-inflammatory properties of 1α,25-dihydroxy-16-ene-20-cyclopropyl-24-oxo-vitamin D3, a Hypocalcemic, stable metabolite of 1α,25-Dihydroxy-16-ene-20-cyclopropyl-vitamin D3. *Journal of Medicinal Chemistry*, *52*, 2204–2213. https://doi.org/10.1021/jm801365a

Li, X.-Y., Boudjelal, M., Xiao, J.-H., Peng, Z.-H., Asuru, A., Kang, S., Fisher, G. J., & Voorhees, J. J. (1999). 1,25-Dihydroxyvitamin D_3 increases nuclear vitamin D_3 receptors by blocking ubiquitin/proteasome-mediated degradation in human skin. *Molecular Endocrinology*, *13*, 1686–1694. https://doi.org/10.1210/mend.13.10.0362

Lilley, E., Stanford, S. C., Kendall, D. E., Alexander, S. P. H., Cirino, G., Docherty, J. R., George, C. H., Insel, P. A., Izzo, A. A., Ji, Y., Panettieri, R. A., Sobey, C. G., Stefanska, B., Stephens, G., Teixeira, M., & Ahluwalia, A. (2020). ARRIVE 2.0 and the British Journal of Pharmacology: Updated guidance for 2020. *British Journal of Pharmacology*, *177*(16), 3611–3616. Portico. https://doi.org/10.1111/bph.15178

Love, M. I., Huber, W., & Anders, S. (2014). Moderated estimation of fold change and dispersion for RNA-seq data with DESeq2. *Genome Biology*, *15*, 550. https://doi.org/10.1186/s13059-014-0550-8

MacKerell, A. D., Bashford, D., Bellott, M., Dunbrack, R. L., Evanseck, J. D., Field, M. J., Fischer, S., Gao, J., Guo, H., Ha, S., Joseph-McCarthy, D., Kuchnir, L., Kuczera, K., Lau, F. T., Mattos, C., Michnick, S., Ngo, T., Nguyen, D. T., Prodhom, B., … Karplus, M. (1998). All-atom empirical potential for molecular modeling and dynamics studies of proteins. *The Journal of Physical Chemistry. B*, *102*, 3586–3616. https://doi.org/10.1021/jp973084f

Murphy, A. B., Nyame, Y., Martin, I. K., Catalona, W. J., Hollowell, C. M. P., Nadler, R. B., Kozlowski, J. M., Perry, K. T., Kajdacsy-Balla, A., & Kittles, R. (2014). Vitamin D deficiency predicts prostate biopsy outcomes. *Clinical Cancer Research*, *20*, 2289–2299. https://doi.org/10.1158/1078-0432.CCR-13-3085

Okamoto, R., Delansorne, R., Wakimoto, N., Doan, N. B., Akagi, T., Shen, M., Ho, Q. H., Said, J. W., & Koeffler, H. P. (2012). Inecalcitol, an

analog of 1α,25(OH)2D3, induces growth arrest of androgen-dependent prostate cancer cells. *International Journal of Cancer*, *130*, 2464–2473. https://doi.org/10.1002/ijc.26279

Otwinowski, Z., & Minor, W. (1997). [20] Processing of X-ray diffraction data collected in oscillation mode. In *Methods in enzymology* (pp. 307–326). Elsevier.

Percie du Sert, N., Hurst, V., Ahluwalia, A., Alam, S., Avey, M. T., Baker, M., Browne, W. J., Clark, A., Cuthill, I. C., Dirnagl, U., Emerson, M., Garner, P., Holgate, S. T., Howells, D. W., Karp, N. A., Lazic, S. E., Lidster, K., MacCallum, C. J., Macleod, M., … Würbel, H. (2020). The ARRIVE guidelines 2.0: Updated guidelines for reporting animal research. *British Journal of Pharmacology*, *177*, 3617–3624. https://doi.org/10.1111/bph.15193

Pérez-García, X., Rumbo, A., Larriba, M. J., Ordóñez, P., Muñoz, A., & Mouriño, A. (2003). The first locked side-chain analogues of calcitriol (1α,25-dihydroxyvitamin D_3) induce vitamin D receptor transcriptional activity. *Organic Letters*, *5*, 4033–4036. https://doi.org/10.1021/ol0351246

Phillips, J. C., Braun, R., Wang, W., Gumbart, J., Tajkhorshid, E., Villa, E., Chipot, C., Skeel, R. D., Kalé, L., & Schulten, K. (2005). Scalable molecular dynamics with NAMD. *Journal of Computational Chemistry*, *26*, 1781–1802. https://doi.org/10.1002/jcc.20289

Rochel, N., Hourai, S., Pérez-García, X., Rumbo, A., Mourino, A., & Moras, D. (2007). Crystal structure of the vitamin D nuclear receptor ligand binding domain in complex with a locked side chain analog of calcitriol. *Archives of Biochemistry and Biophysics*, *460*, 172–176. https://doi.org/10.1016/j.abb.2007.01.031

Scher, H. I., Jia, X., Chi, K., de Wit, R., Berry, W. R., Albers, P., Henick, B., Waterhouse, D., Ruether, D. J., Rosen, P. J., Meluch, A. A., Nordquist, L. T., Venner, P. M., Heidenreich, A., Chu, L., & Heller, G. (2011). Randomized, open-label phase III trial of docetaxel plus high-dose calcitriol versus docetaxel plus prednisone for patients with castration-resistant prostate cancer. *Journal of Clinical Oncology*, *29*, 2191–2198. https://doi.org/10.1200/JCO.2010.32.8815

Schindelin, J., Arganda-Carreras, I., Frise, E., Kaynig, V., Longair, M., Pietzsch, T., Preibisch, S., Rueden, C., Saalfeld, S., Schmid, B., Tinevez, J. Y., White, D. J., Hartenstein, V., Eliceiri, K., Tomancak, P., & Cardona, A. (2012). Fiji: An open-source platform for biological-image analysis. *Nature Methods*, *9*, 676–682. https://doi.org/10.1038/nmeth.2019

Siddappa, M., Hussain, S., Wani, S. A., White, J., Tang, H., Gray, J. S., Jafari, H., Wu, H. C., Long, M. D., Elhussin, I., Karanam, B., Wang, H., Morgan, R., Hardiman, G., Adelani, I. B., Rotimi, S. O., Murphy, A. R., Nonn, L., Davis, M. B., … Campbell, M. J. (2023). African American prostate cancer displays quantitatively distinct vitamin D receptor Cistrome-transcriptome relationships regulated by BAZ1A. *Cancer Research Communications*, *3*, 621–639. https://doi.org/10.1158/2767-9764.CRC-22-0389

Siegel, R. L., Giaquinto, A. N., & Jemal, A. (2024). Cancer statistics, 2024. *CA a Cancer J Clinicians*, *74*, 12–49. https://doi.org/10.3322/caac.21820

Sigüeiro, R., Maestro, M. A., & Mouriño, A. (2018). Synthesis of side-chain locked analogs of 1α,25-dihydroxyvitamin D_3 bearing a C17 methyl group. *Organic Letters*, *20*, 2641–2644. https://doi.org/10.1021/acs.orglett.8b00849

Smart, O. S., Womack, T. O., Flensburg, C., Keller, P., Paciorek, W., Sharff, A., Vonrhein, C., & Bricogne, G. (2012). Exploiting structure similarity in refinement: Automated NCS and target-structure restraints in *BUSTER*. *Acta Crystallographica. Section D, Biological Crystallography*, *68*, 368–380. https://doi.org/10.1107/S0907444911056058

Tanaka, Y., DeLuca, H. F., Kobayashi, Y., & Ikekawa, N. (1984). 26,26,26,27,27,27-Hexafluoro-1,25-dihydroxyvitamin D3: A highly potent, long-lasting analog of 1,25-dihydroxyvitamin D3. *Archives of Biochemistry and Biophysics*, *229*, 348–354. https://doi.org/10.1016/0003-9861(84)90161-9

Ting, H.-J., Hsu, J., Bao, B.-Y., & Lee, Y.-F. (2007). Docetaxel-induced growth inhibition and apoptosis in androgen independent prostate cancer cells are enhanced by 1α,25-dihydroxyvitamin D3. *Cancer Letters*, *247*, 122–129. https://doi.org/10.1016/j.canlet.2006.03.025

Trump, D. L. (2018). Calcitriol and cancer therapy: A missed opportunity. *Bone Reports*, *9*, 110–119. https://doi.org/10.1016/j.bonr.2018.06.002

Trump, D. L., & Aragon-Ching, J. B. (2018). Vitamin D in prostate cancer. *Asian Journal of Andrology*, *20*, 244–252. https://doi.org/10.4103/aja.aja_14_18

Väisänen, S., Dunlop, T. W., Sinkkonen, L., Frank, C., & Carlberg, C. (2005). Spatio-temporal activation of chromatin on the human CYP24 gene promoter in the presence of 1α,25-dihydroxyvitamin D3. *Journal of Molecular Biology*, *350*, 65–77. https://doi.org/10.1016/j.jmb.2005.04.057

Vanhevel, J., Verlinden, L., Loopmans, S., Doms, S., Janssens, I., Bevers, S., Stegen, S., Wildiers, H., & Verstuyf, A. (2022). The combination of the CDK4/6 inhibitor, Palbociclib, with the vitamin D3 analog, Inecalcitol, has potent in vitro and in vivo anticancer effects in hormone-sensitive breast cancer, but has a more limited effect in triple-negative breast cancer. *Frontiers in Endocrinology*, *13*, 886238. https://doi.org/10.3389/fendo.2022.886238

Yanagisawa, T., Kawada, T., Rajwa, P., Mostafaei, H., Motlagh, R. S., Quhal, F., Laukhtina, E., König, F., Pallauf, M., Pradere, B., Karakiewicz, P. I., Nyirady, P., Kimura, T., Egawa, S., & Shariat, S. F. (2023). Sequencing impact and prognostic factors in metastatic castration-resistant prostate cancer patients treated with cabazitaxel: A systematic review and meta-analysis. *Urologic Oncology*, *41*, 177–191. https://doi.org/10.1016/j.urolonc.2022.06.018

Yu, G., Wang, L.-G., Yan, G.-R., & He, Q.-Y. (2015). DOSE: An R/-bioconductor package for disease ontology semantic and enrichment analysis. *Bioinformatics*, *31*, 608–609. https://doi.org/10.1093/bioinformatics/btu684

SUPPORTING INFORMATION

Additional supporting information can be found online in the Supporting Information section at the end of this article.

How to cite this article: Len-Tayon, K., Beraud, C., Fauveau, C., Belorusova, A. Y., Chebaro, Y., Mouriño, A., Massfelder, T., Chauchereau, A., Metzger, D., Rochel, N., & Laverny, G. (2024). A vitamin D-based strategy overcomes chemoresistance in prostate cancer. *British Journal of Pharmacology*, 1–15. https://doi.org/10.1111/bph.16492